J. Korean Inst. Electr. Electron. Mater. Eng.
Vol. 38, No. 2, pp. 226-231 March 2025
doi: https://doi.org/10.4313/JKEM.2025.38.2.15
ISSN 1226-7945(Print), 2288-3258(Online)

Early Stage Report : Graduate Research

Electrical Characteristics of Bifacial OPVs Based on Ultrasonically Controlled Printing Process of a Non-Contact Method

Sunyoung Sohn

Department of Electrical and Electronic Engineering, Sangji University, Wonju 26339, Korea

(Received December 3, 2024; Revised December 4, 2024; Accepted December 5, 2024)

Abstract: The printed and bifacial organic photovoltaics (OPVs) using a semi-transparent electrode structure to enhance light management were investigated. To optimize energy-band alignment for bifacial device structure, a cathode interlayer of ZnO nanoparticles with a low work function of 3.9 eV combined with a polyethyleneimine (PEI) layer was employed. Photon distribution simulations revealed the influence of structural parameters on device conductivity, light absorption, and surface morphology. The dispensing strength, adjusted via applied voltage during printing, significantly impacted device performance. At 13 V and 17 V, *J-V* characteristics were consistent; however, at 20 V, line width increased by approximately 100%, resulting in a 50% reduction in *PCE*. These findings highlight the critical relationship between spraying strength, line width, and efficiency, offering valuable insights for advancing printed OPV technologies.

Keywords: Organic photovoltaic, Printing, Bifacial, Interlayer, Photon distribution

Organic photovoltaics (OPVs) represent a promising class of solar energy technologies due to their unique advantages such as lightweight structure, mechanical flexibility, and tunable optical properties [1]. Among these, the development of printed OPVs has drawn significant attention as it enables scalable, cost-effective, and eco-friendly production as well as easy-to-solution processes. These methods not only facilitate the fabrication of large-area devices but also align with the growing demand for sustainable energy solutions by minimizing material waste and energy-intensive processes. Printed OPVs, therefore, have the potential to transform energy production in both rural and urban environments, offering a versatile alternative to traditional silicon-based photovoltaics [2].

✉ **Sunyoung Sohn; sysohn@sangji.ac.kr**

Bifacial OPVs, which are comparable to an extension of conventional OPVs, provide an innovative approach to further enhance the efficiency and energy yield of organic solar cells. Unlike their single-junction counterparts, bifacial OPVs are capable of harvesting light from both the front and rear surfaces, thereby capturing diffuse and reflected light [3,4]. This capability makes them highly suitable for deployment in environments with high levels of indirect sunlight, such as urban canopies, building facades, and agricultural fields. By combining the benefits of bifacial architectures with the versatility of printed fabrication techniques, researchers are paving the way for next-generation photovoltaics that maximize energy generation across diverse applications. The synergy of the printing process and bifacial OPVs thus offers a dual advantage: scalable production and increased energy output. Printing technology has shown significant promise for fabricating OPVs due to its advantages of being a contactless, maskless process with high material utilization and compati-

bility with roll-to-roll production. These characteristics enable the production of lightweight, flexible, and scalable solar cells, ideal for diverse applications, including energy-integrated designs [5,6]. Roll-to-roll techniques, combined with slot-die or inkjet printing, have been pivotal in advancing flexible OPVs [7]. These processes support the fabrication of large-area devices with reduced costs and environmental impact, a crucial research step for commercialization. The Microplotter printing system employs ultrasonic pumping mediated by piezoelectric actuators to enable precision fluid dispensing at the microscale. This advanced technique accommodates a broad range of viscosities, allowing the deposition of functional layers with high uniformity and tailored film properties [8-10]. Critical parameters such as spray intensity, tip height, and patterning speed were systematically investigated to optimize the morphology, thickness, and optical properties of the deposited films. In this study, the Microplotter system was utilized for precise fluid dispensing, leveraging a piezoelectric actuator integrated into the dispenser. Upon the application of alternating current to the piezoelectric element, mechanical vibrations are induced. When these vibrations reach a critical amplitude at the system's resonant frequency, the resulting energy facilitates the ejection of the solution as a fine spray from the nozzle tip, ensuring controlled deposition. Bifacial organic photovoltaics present a significant advancement over traditional single-junction OPVs by exploiting reflected and diffused sunlight to enhance energy harvesting. Key design parameters, including ground albedo, device height, and tilt angle, influence their ability to achieve superior efficiencies.

This study employed a semi-transparent electrode structure to improve light management in inverted bifacial OPVs. A cathode interlayer of ZnO nanoparticles with a low work function of 3.9 eV, combined with a polyethyleneimine (PEI) layer, was introduced to optimize energy-band alignment for inverted bifacial device structure. Simulations of photon distribution provided further insights into the effects of structural parameters on the device's conductivity, light absorption, and surface morphology.

Figures 1(a) and (b) are a schematic diagram of the spin-coated OPV device structure and the electrical characteristics. The 150 nm thick indium tin oxide (ITO) glass substrate as the anode was ultrasonically cleaned using acetone, 2-propanol (IPA), and DI-water for 10 minutes each. After drying at 90°C for 1 hour to remove any residual solvent components remaining on the surface, the device was fabricated. To improve the hydrophilicity of the ITO substrate before coating the thin film, UV surface treatment was performed for 30 minutes. After that, poly(3,4-ethylenedioxythiophene):poly (styrenesulfonate) (PEDOT:PSS) was spin-coated as a hole transport layer on the ITO substrate using a spin-coating device at 2,000 rpm for 50 seconds, and then a 30 nm film was formed by post-heat treatment at 150°C for 30 minutes. The poly(3-hexylthiophene-2,5-diyl) (P3HT) and fullerene derivatives [6,6]-Phenyl-C71-butyric acid methyl ester ($PC_{70}BM$) blend used as the photoactive layer was mixed in a 1:1 ratio and mixed in chlorobenzene (CB) solvent for 24 hours. P3HT:$PC_{70}BM$ was spin-coated on the hole transport layer at 1,500 rpm for 50 seconds, and then a 150 nm film was formed through a post-heat treatment process at 120°C for 30 minutes. LiF interlayer (1 nm) and Al cathode (100 nm) were thermally evaporated, respectively. For comparison between spin-coated and printed device performance, the schematic diagram of the printed device structure and the electrical characteristics of the printed OPVs are shown in Figs. 1(c) and (d). The chemical structures for spin-coated and printed OPVs fabrication. In this paper, the printing process was performed using the MicroplotterTM Pro model from SonoPlot. The Microplotter printer includes a positioning system with a print head and an optical system, and a control electronics device. In addition, it has the advantage of being able to efficiently control the dispenser by adjusting various printing parameters such as spray intensity and speed. The electrical characteristics of the OPVs were measured using a Keithley 2634B source meter under AM 1.5 G, 100 mW/cm² conditions. To analyze the changes in optical properties of the bifacial device structure compared to the conventional device with the light incidence to bottom side in structure, we used OghmaNano simulation.

The electrical characteristics of the spin-coated devices were analyzed a short-circuit current-density (J_{sc}, 0.75 mA/cm^2), open-circuit voltage (V_{oc}, 0.56 V), fill-factor (*FF*, 53.55), power-conversion efficiency (*PCE*, 3.5%), as shown in Fig. 1(b). When the dispensing strength in the printed devices was 13 V or 17 V, similar J-V curves were shown, but on the other hand, when the spraying strength was 20, the increase rate greatly increased to about 100%, which resulted in the PCE decreased by 50%. The current-density versus

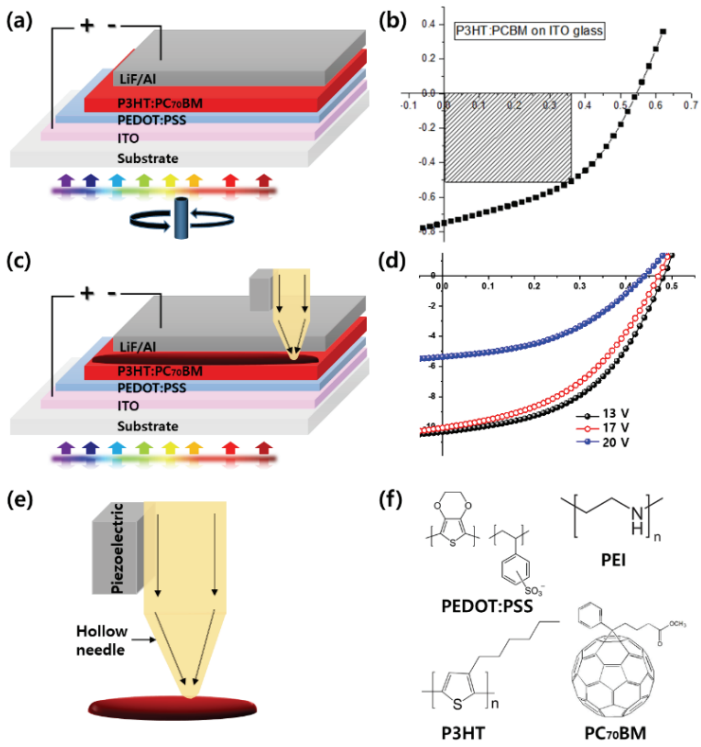

Fig. 1. Schematic of (a) spin-coated device structure and (b) current-voltage characteristic. Schematic of (c) printed device structure and (d) current density-voltage characteristic with different printing strengths. (e) Schematic of fluid coating via ultrasonic pumping using Microplotter system, and (f) chemical structures of buffer and active materials.

Table 1. Electrical characteristics of printed conventional OPVs with different printing strengths.

Strength (V)	J_{sc}[a] (mA/cm^2)	V_{oc}[b] (V)	Jm[c] (mA/cm^2)	V_m[d] (V)	FF[e]	PCE[f] (%)
13	10.34	0.49	7.46	0.32	47.16	2.39
17	10.06	0.48	7.02	0.30	43.6	2.11
20	5.37	0.45	3.64	0.28	42.12	1.02

[a]J_{sc}: Short circuit current density, [b]V_{oc}: Open-circuit voltage, [c]J_m: Maximum current density, [d]V_m: Maximum voltage, [e]FF: Fill factor, [f]PCE: Power-conversion efficiency

voltage characteristic are measured and electrical parameters are listed in Table 1 with different printing strengths of 13, 17, and 20 V. In the case of the Microplotter printer, the 'dispensing strength' was adjusted to control the spraying strength applied during printing when performing dispenser control, and the line width was controlled by adjusting the driving voltage within the range of 1 to 20 V. When the applied voltage was in the range of 13 to 15 V, but the line width gradually increased as the spraying strength increased, and in particular, when the applied voltage increased to 20 V, the increase rate greatly increased to about 100%. Photon distribution in OPVs refers to the spatial and spectral distribution of incident light within the device, as shown in Fig. 2(a). It is influenced by factors such as the refractive index and thickness of the layers, as well as any nanostructure. From these simulations, it could be predicted how use optical transfer matrix methods or finite-difference time-domain modeling to photons propagate through the multilayer structure [11]. The interference effects between reflected and transmitted light waves result in specific intensity profiles, crucial for optimizing absorption. Absorbed photon distribution quantifies the regions within the OPV where incident photons could be converted into excitons [11,12]. These depends on the active layer's absorption coefficient and the electric field strength in different layers. In conventional OPVs, the bulk heterojunction layer is designed to maximize light absorption. Simulations calculate the absorption profile using Maxwell's equations to evaluate how material properties

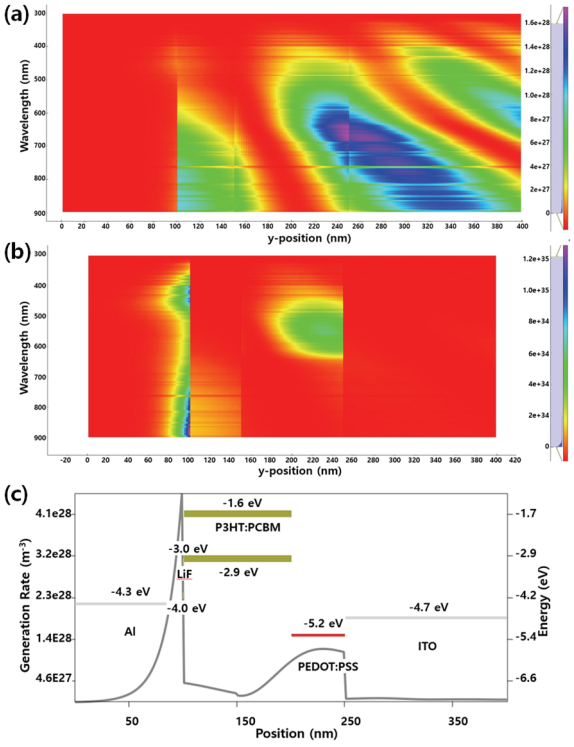

Fig. 2. (a) Photon distribution, (b) photon distribution absorbed, and (c) generation rate of simulated OPVs with conventional device structure.

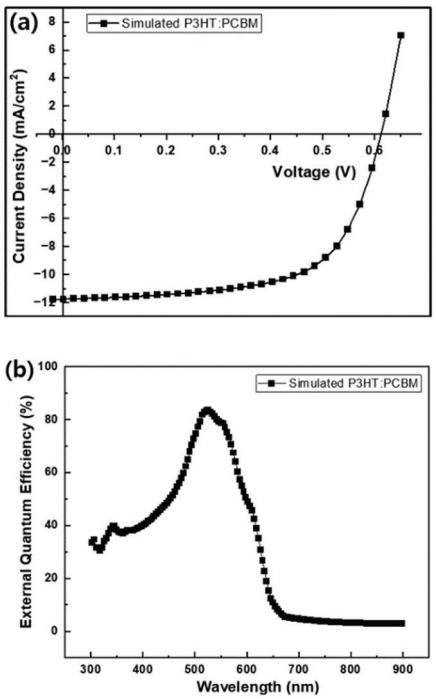

Fig. 3. Simulated conventional OPVs (a) current density versus voltages and (b) external quantum efficiency.

and layer thicknesses affect light trapping and conversion efficiency. The electrical parameters of the simulated device shows J_{sc} (11.76 mA/cm^2), V_{oc} (0.61 V), *FF* (62.1), and *PCE* (4.45%), as depicted in Figs. 3(a) and (b). When comparing the electrical characteristic measurement results of the simulated device with the experimental results, J_{sc} and V_{oc} except for *FF* show comparable values. Various *FF* value arise from several factors related to the internal and external mechanisms that govern charge generation, transport, and extraction. The resistance comes from low conductivity of the active layer, imperfect charge transport layers, and contact resistance at the electrode/active interface. High series resistance could reduce the *FF* by limiting current flow [13,14]. Charge recombination before charges reach the electrodes reduces *FF*, which is caused by the poor separation of exciton into free charge carriers and imbalance in electron and hole mobility. Improper energy-band alignment between the active layer and electrode materials can hinder charge extraction by work-function mismatch or inadequate inter-facial layers [15]. Unbalanced phase separation or morphology can reduce charge mobility and extraction efficiency, lowering *FF*. It is caused by the inhomogeneous blending of donor and acceptor materials and annealing or solvent drying conditions [16]. Material degradation over time (e.g., oxidation, UV damage) can lower *FF* by introducing traps or increasing resistances [17]. Figure 4(a) is a schematic diagram of a bifacial device structure towards both light incident bottom and top direction with semi-transparent Ag metal. The current-density versus voltages of OPVs with (b) filtered-ZnO nanoparticle and (c) 20% ethanol diluted-ZnO nanoparticle are shown in Fig. 4, and their electrical parameters are listed in Table 2. The devices with two interlayers exhibit similar properties, but when ethanol-diluted ZnO is used as an interlayer, a slightly increased J_{sc} value is shown due to improved nanoparticle dispersion. Moreover, balanced electron and hole mobility reduce charge accumulation and recombination at the interfaces, directly enhancing *FF* value. In Fig. 5, reduced parasitic absorption in the semi-transparent electrodes and optimized optical stack in bifacial OPVs reduce parasitic absorption by non-active layers. This improves the optical electric field distribution in the active layer, leading to efficient carrier generation and collection. Simulated bifacial

Table 2. Electrical characteristics of printed bifacial OPVs according to the direction of light incidence or interface layers.

Light incident	Interlayer	J_{sc} (mA/cm^2)	V_{oc} (V)	Jm (mA/cm^2)	V_m (V)	FF	PCE (%)
Au (top)	ZnO	3.65	0.47	2.607	0.31	47.1	0.81
ITO (bottom)	ZnO	10.246	0.50	6.454	0.29	36.39	1.89
Au (top)	ZnO 20%@ethanol	5.099	0.46	3.175	0.29	39.27	0.93
ITO (bottom)	ZnO 20%@ethanol	10.94	0.50	6.720	0.31	37.78	2.07

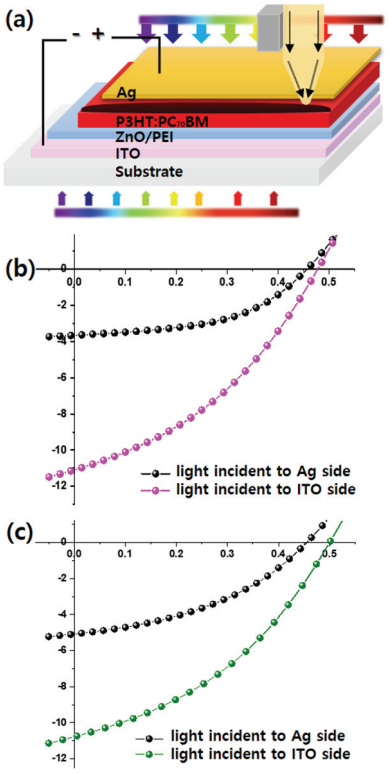

Fig. 4. (a) Bifacial device structure with light in both incident bottom and top direction. Current density versus voltages of OPVs with (b) filtered-ZnO nanoparticle, and (c) 20% ethanol diluted-ZnO nanoparticle.

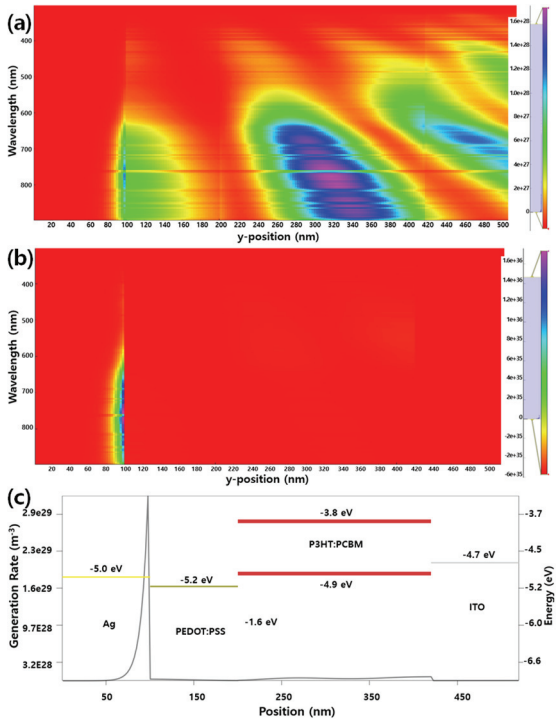

Fig. 5. (a) Photon distribution, (b) photon distribution absorbed, and (c) generation rate of simulated bifacial OPVs.

OPVs exhibit the J_{sc} (11.76 mA/cm^2), V_{oc} (0.61 V), *FF* (62.8), *PCE* (4.50%), as depicted in Fig. 6(a). The increased *FF* performance observed in bifacial OPV devices compared to conventional OPV devices of Fig. 3(a) can be attributed to several factors inherent to the design and operation of bifacial devices by the enhanced light utilization. In general dual-sided light absorption, the bifacial OPVs utilize light incident from both the front and rear sides, increasing the effective photon flux. Improved photon harvesting can lead to higher photo-generated carrier densities, reducing recombination losses and enhancing *FF*. These improved energy-band alignment with bifacial OPV designs often incorporate advanced interfacial layers that optimize energy-band alignment between the electrodes and the active layer. This alignment minimizes charge extraction barriers, reduces resistive losses, and improves *FF*. Therefore, balanced charge transport in the symmetric structure of bifacial OPVs can lead to more uniform charge transport and extraction compared to conventional devices. Bifacial OPVs can absorb light from both sides, enabling their integration into vehicle roofs and sides for efficient light harvesting and electricity generation during transit. Moreover, when deployed in agricultural applications,

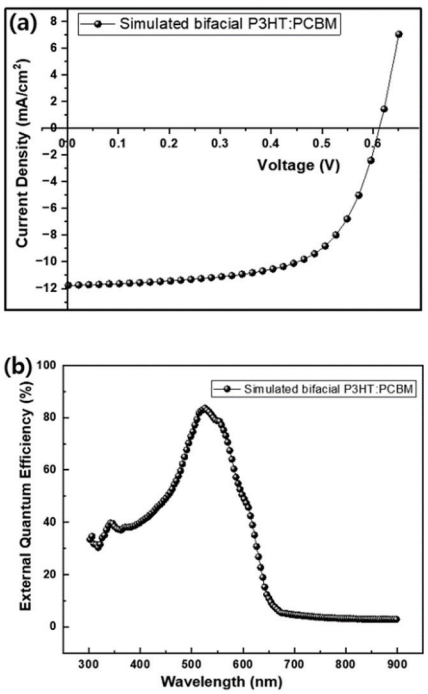

Fig. 6. (a) Current-density versus voltages and (b) external quantum efficiency of simulated bifacial OPVs.

bifacial solar cells can capture not only the light reflected from the crop canopy but also from the ground, which is expected to optimize space utilization, thereby supporting crop growth and generating renewable energy.

ORCID

Sunyoung Sohn https://orcid.org/0000-0002-5543-627X

ACKNOWLEDGEMENT

This research was supported by the Sangji University research grant for the academic year 2022.

REFERENCES

[1] N. Chandrasekaran, A. Kumar, L. Thomsen, D. Kabra, and C. R. McNeill, *Mater. Adv.*, **2**, 2045 (2021).
doi: https://doi.org/10.1039/d0ma00738b

[2] J. Liu, Y. Li, M. Li, S. Arumugam, and S. P. Beeby, *IEEE J. Photovoltaics*, **9**, 1020 (2019).
doi: https://doi.org/10.1109/JPHOTOV.2019.2899432

[3] H. Li, Y. Wang, H. Gao, M. Zhang, R. Lin, P. Wu, K. Xiao, and H. Tan, *eLight*, **2**, 21 (2022).
doi: https://doi.org/10.1186/s43593-022-00028-w

[4] J. Barichello, P. Mariani, L. Vesce, D. Spadaro, I. Citro, F. Matteocci, A. Bartolotta, A. Di Carlo, and G. Calogero, *J. Mater. Chem. C*, **12**, 2317 (2023).
doi: https://doi.org/10.1039/d3tc03220e

[5] C. Amruth, B. Luszcynska, B.G.R. Dupont, and Z. Sieradzki, *Disp. Imaging*, **2**, 339 (2017).

[6] S. K. Karunakaran, G. M. Arumugam, W. Yang, S. Ge, S. N. Khan, X. Lin, and G. Yang, *J. Mater. Chem. A*, **7**, 13873 (2019).
doi: https://doi.org/10.1039/c9ta03155c

[7] S. Sumaiya, K. Kardel, and A. El Shahat, *Proc. 2017 IEEE SmartWorld, Ubiquitous Intelligence & Computing, Advanced & Trusted Computed, Scalable Computing & Communications, Cloud & Big Data Computing, Internet of People and Smart City Innovation (SmartWorld/SCALCOM/UIC/ATC/CBDCom/IOP/SCI)* (IEEE, San Francisco, USA, 2018) p. 1.
doi: https://doi.org/10.1109/UIC-ATC.2017.8397439

[8] Q. Li and J. Liu, *Adv. Electron. Mater.*, **6**, 2000537 (2020).
doi: https://doi.org/10.1002/aelm.202000537

[9] X. Fang, J. Shi, X. Zhang, X. Ren, B. Lu, W. Deng, J. Jie, and X. Zhang, *Adv. Funct. Mater.*, **31**, 2100237 (2021).
doi: https://doi.org/10.1002/adfm.202100237

[10] H. Kang, H. Jeong, S. Hong, N. K. Yoon, and S. Sohn, *J. Korean Inst. Electr. Electron. Mater. Eng.*, **37**, 382 (2024).
doi: https://doi.org/10.4313/JKEM.2024.37.4.4

[11] A. Fiore, C. Bevilacqua, and G. Scarcelli, *Phys. Rev. Lett.*, **122**, 103901 (2019).
doi: https://doi.org/10.1103/PhysRevLett.122.103901

[12] M. H. Shachar, G. Uahengo, E. H. Penilla, Y. Kodera, and J. E. Garay, *J. Appl. Phys.*, **128**, 083103 (2020).
doi: https://doi.org/10.1063/5.0014937

[13] N. Mundhaas, Z. J. Yu, K. A. Bush, H. P. Wang, J. Häusele, S. Kavadiya, M. D. McGehee, and Z. C. Holman, *Sol. RRL*, **3**, 1800378 (2019).
doi: https://doi.org/10.1002/solr.201800378

[14] P. Subudhi and D. Punetha, *Sci. Rep.*, **13**, 19485 (2023).
doi: https://doi.org/10.1038/s41598-023-33419-1

[15] H. F. Haneef, A. M. Zeidell, and O. D. Jurchescu, *J. Mater. Chem. C*, **8**, 759 (2020).
doi: https://doi.org/10.1039/c9tc05695e

[16] A. Karki, J. Vollbrecht, A. J. Gillett, S. S. Xiao, Y. Yang, Z. Peng, N. Schopp, A. L. Dixon, S. Yoon, M. Schrock, H. Ade, G.N.M. Reddy, R. H. Friend, amd T. Q. Nguyen, *Energy Environ. Sci.*, **13**, 3679 (2020).
doi: https://doi.org/10.1039/d0ee01896a

[17] A. Sinha, J. Qian, S. L. Moffitt, K. Hurst, K. Terwilliger, D. C. Miller, L. T. Schelhas, and P. Hacke, *Prog. Photovoltaics: Res. Appl.*, **31**, 36 (2023).
doi: https://doi.org/10.1002/pip.360